1 **The use of ASH-15 flowstone as a matrix-matched reference material for laser-ablation**

2 **U-Pb geochronology of calcite**

3 Perach Nuriel[1], Jörn-Frederik Wotzlaw[2], Maria Ovtcharova[3], Anton Vaks[1], Ciprian Stremtan[4],

4 Martin Šala[5], Nick M. W. Roberts[6], and Andrew R. C. Kylander-Clark[7]

6 [1] Geological Survey of Israel, 32 Yeshayahu Leibowitz St. Jerusalem, 9692100, Israel

7 [2] Institute of Geochemistry and Petrology, ETH Zurich, Clausiusstrasse 25 I CH-8092 Zurich,

8 Switzerland

9 [3] Department of Earth Sciences, University of Geneva, Geneva, Switzerland

10 [4] Teledyne Photon Machines, 384 Gallatin Park Drive, Bozeman, MT 59715, USA

11 [5] Department of Analytical Chemistry, National Institute of Chemistry, Hajdrihova 19, SI-

12 1000 Ljubljana, Slovenia.

13 [6] Geochronology and Tracers Facility, British Geological Survey, Environmental Science

14 Centre, Nottingham, NG12 5GG, UK

15 [7] Department of Earth Science, University of California, Santa Barbara, CA 93106, USA.

17 **Abstract**

18 Latest advances in laser ablation inductively coupled plasma mass spectrometer (LA-ICPMS)

19 allow for accurate *in-situ* U-Pb dating of carbonate material, with final age uncertainties

20 usually >3% 2σ. Cross-laboratory reference materials (RMs) used for sample-bracketing are

21 currently limited to WC1 calcite with an age of 254.4 ± 6.5 (2σ). The minimum uncertainty

22 on any age determination with the LA-ICPMS method is therefore ≥ 2.5%, and validation by

23 secondary RMs are usually performed on in-house standards. This contribution present a new

24 reference material, ASH-15, a flowstone that is dated here by high-precision Isotope Dilution

25 (ID) TIMS analysis using 36 sub-samples, 1-7 mg each. Age results presented here are

26 slightly younger compared to previous ID dating of ASH-15, but in agreement with *in-situ*

27 analyses (using WC1 as a RM). We provide new correction parameters to be used as primary

28 or secondary standardization. The suggested $^{238}U/^{206}Pb$ apparent age, not corrected for

29 disequilibrium and without common-lead anchoring, is 2.965 ± 0.011 Ma (2σ). The new

30 results could improve the propagated uncertainties on the final age with a minimal value of

31 0.4%, which is approaching the uncertainty of typical ID analysis on, for example, zircon

32 (<1% 2s). We show that although LA-ICPMS spot analyses of ASH-15 exhibits significant

33 scatter in their isotopic ratios, the down-hole fractionation of ASH-15 is similar to that of

34 other reference materials. For LA work, we recommend the use of the new ID-TIMS ages

35 that are 1.3-1.5% younger than previously suggested, because of the lower uncertainties

36 (0.4%), the large number of sub-samples (n=36), the use of the EARTHTIME isotopic tracers,

37 and the small aliquots (1-7 mg) that are more representative of laser-ablation spot analysis.

38 **1. Introduction**

39 Recent advances in laser ablation techniques applied to multi-phase carbonates allow for

40 accurate dating of a variety of sample types, including calcite cements (Li et al., 2014;

41 Godeau et al., 2018; Anjiang et al., 2019; Holdsworth et al., 2019), hydrothermal veins

42 (Coogan et al., 2016; MacDonald et al., 2019; Piccione et al., 2019), fault-related veins,

43 breccia cement, and slickenfibers (Ring and Gerdes, 2016; Roberts and Walker, 2016; Nuriel

44 et al., 2017; Hansman et al., 2018; Parrish et al., 2018; Nuriel et al., 2019), and speleothems

45 (Woodhead and Petrus, 2019). With increasing attention on climatic, seismic, and

46 environmental events in the geological record there is a growing need for dating techniques

47 that can be accurately and easily implemented to samples at the sub-millimeter scale. This

48 newly emerging technique has the potential to contribute to our understanding of the duration,

49 rate, and extent of these important events in the geological record.

50 The *in-situ* approach has a great research potential for studying texturally complex samples

51 because it can resolve problems of age mixing of different phases or averaging of continuous

52 growth at the sub-millimeter scale, and thus increase the overall accuracy of the dated

53 material. While the precision of traditional isotope-dilution (ID) U-Pb analyses is still

54 favorable (<1% 2σ) (Woodhead and Petrus, 2019), increasing analytical development of the

55 LA-ICPMS method indicates the potential for improving the currently reported uncertainties

56 (usually >3% 2σ). Finding the right matrix-matched reference material (RM) is a major

57 hurdle for LA analyses of carbonates because of the variety of mineralogy (calcite, dolomite,

58 and aragonite), textures, composition (e.g. high-magnesium calcite, high common-lead), and

59 ages (e.g. low radiogenic lead in young samples). Textural differences such as

60 microcrystalline, fine- and coarse-grained material, between the unknown and RMs can

61 contribute to high uncertainties due to differences in ablation efficiency, down-hole

62 fractionation, and differences in crater morphology (e.g. Guillong et al., 2020 and Elisha et al,

63 2020, this issue). Observed deviations are potentially up to 20% of the final intercept age

64 depending on the degree of crater geometry mismatch and are related to either to downhole

65 fractionation and/or matrix effects (Guillong et al., 2020).

66 Currently, the most commonly used procedure for mass-bias correction in the LA method, is

67 by standard-sample bracketing. For this, the $^{238}U/^{206}Pb$ LA-age of the RMs is corrected to the

68 true RM's $^{238}U/^{206}Pb$ apparent age (not corrected for disequilibrium) as measured

69 independently by an ID method (e.g. ID-TIMS). The RMs are measured throughout each

70 session along with the unknown samples, and a normalization factor is applied to correct both

71 the RMs and the unknowns. Uncertainty propagation onto the age of the unknowns includes

72 the uncertainties of the 'true' RM age. As a result, the accuracy of the LA analyses can only

73 be as good as the uncertainties on the age of the RMs which is by itself subjected to analytical

74 challenges due to natural heterogeneities, impurities, and textural complexities at the sub-

75   millimetre scale. It is therefore essential that the 'true age' of the reference material will

76   reflect these complexities while maintaining minimal uncertainties.

77   Currently, several in-house standards are being used as reference materials, including Duff

78   Brown Tank (64 Ma; Hill et al., 2016), and JT (13.797 ± 0.031 Ma; Guillong et al., 2020).

79   The only well-characterized reference material that is distributed across laboratories is the

80   WC1 calcite with an age of 254.4 ± 6.5 2s (2.5%) (Roberts et al., 2017). The use of WC1

81   alone for mass-bias correction has several disadvantages. First, it is highly recommended

82   with all in situ U-Th-Pb geochronology to use secondary RMs to validate any correction

83   parameters that are being used, and to appropriately propagate uncertainties. Second, the

84   relatively high uncertainty (2.5%) on the age of WC1 sets a minimal uncertainty on any LA

85   U-Pb age determination. Finally, the quantity of the WC1 sample that is currently available

86   for future work is limited and is likely to not fully meet the growing demands of the LA

87   scientific community; although, we note here that there is a potential for further sample

88   collection from the original site.

89   This contribution introduces a new carbonate reference material that can be widely used for

90   *in-situ* dating of calcite as primary or as cross-reference material with other available

91   standards. We characterise the reference material at various resolutions using a combination

92   of (1) laser ablation imaging (20 μm square beam); (2) LA spot analysis, ~80-110 μm in

93   diameter, conducted on both multi-collector (MC) and single collector inductively coupled

94   plasma mass spectrometer (ICPMS); and (3) ID-TIMS analyses of 36 sub-samples ~1-7 mg

95   aliquots. We discuss several key issues related to the use of ASH-15 sample as a RM,

96   including down-hole fractionation, heterogeneities, previous bulk analyses, and the possible

97   effect of samples size and blank corrections, to provide the best correction parameters and

98   suggested protocols for users of the LA scientific community.

2. The ASH-15 flowstone

The ASH-15 flowstone was found in Ashalim Cave, a karstic cave in the central Negev Desert (30°56′36.2″ N, 34°44′22.5″ E), southern Israel, which is part of the northern margin of the Saharan–Arabian desert belt. The cave entrance is located at an elevation of 414 m above sea level and 67 km SE from the Mediterranean Sea coast. The cave is a three-dimensional hypogene maze with a total length of 540 m, situated in Turonian limestone rock strata, at depths of 0-31 m below the surface. The cave is richly decorated with vadose speleothems, such as stalagmites, stalactites and flowstone, which are not active today because of the aridity of the climate in the area (Vaks et al, 2010, 2018), but periods of their deposition correspond to past episodes of wet climate in present-day desert The thickness of the speleothems varies from several cm to a few tens of cm. The soil above the cave is silicate loess, originated mainly from aeolian dust (Crouvi et al., 2010) and the present day vegetation is composed of sparse xeric shrubs with <10% vegetation cover.

The vadose speleothems of Ashalim Cave are composed of low-Mg calcite, and are divided into a relatively thick Pliocene Basal layer, and thinner Pleistocene layers above it. The Basal layer varies from 5 to 25 cm in thickness and comprises c. 90% of the speleothem volume in the cave. It is composed of massive yellow calcite crystals (Fig. 1a-b), often showing continuous growth in stalagmites and flowstone, suggesting deposition from continuously dripping water. In all speleothems the Basal layer is terminated at its top by a <1 mm layer of microcrystalline calcite, evaporite minerals and reddish clays (Fig. 1a), that is interpreted as a hiatus (growth break) separating the Basal Pliocene layer and Quaternary layers above it (Vaks et al., 2013). The thickness of Pleistocene top layers varies from several mm to 17 cm, but usually does not exceed a few cm, comprising about 10% of the speleothem volume in the cave. It is composed of alternating layers of brown calcite, with the youngest top layer (where found) composed of yellow calcite. Several variably colored layers <1 mm thick of

124   microcrystalline calcite, evaporite minerals and reddish clays are found within the columnar

125   crystalline structure, suggesting hiatuses in speleothem deposition (Vaks et al., 2013).

126   The youngest periods of speleothem deposition in several Ashalim Cave speleothems were

127   dated by U-Th method and occurred from 221 ka to 190 ka and from 134 to 114 ka (Vaks et

128   al, 2010). Earlier periods of deposition were dated by the U-Pb method on ASH-15 flowstone

129   and are dated to 1.272 ± 0.018 Ma (ASH-15-C), and the Basal layer of ASH-15 flowstone

130   (layers D-K) dated to c. ~3.1 Ma (Fig 1a). These layers have been dated in three different labs

131   following several protocols for ID analysis (Vaks et al., 2013; Mason et al., 2013). The U

132   concentrations in speleothem calcite range between 1.9 and 19.7 µg/g and the amounts of

133   non-radiogenic Th are negligible (Vaks et al., 2010).
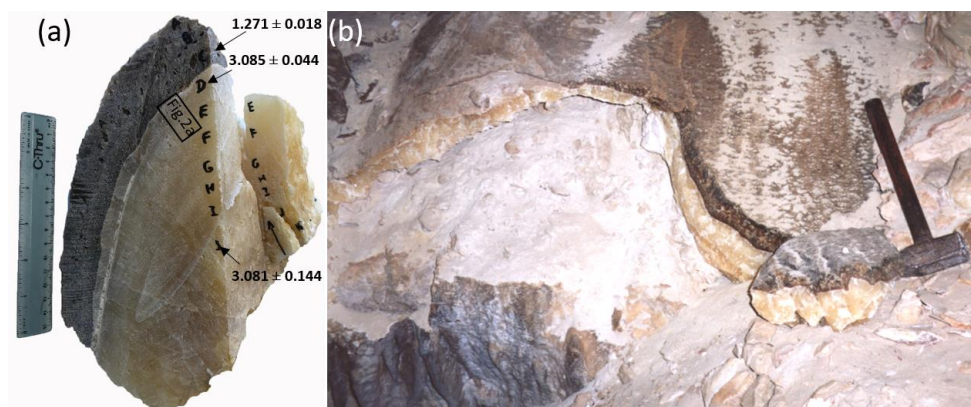
134

135   **Figure 1.** Sample ASH-15 from Ashalim Cave. (a) ~5 kg block of sample ASH-15 flowstone

136   consisting of the massive Pliocene yellow Basal layer (>2 cm calcite crystals; section D–K)

137   and the brown Quaternary layer (top section, A–C), the thin layer between the two

138   stratigraphic members represents a growth break (hiatus). The main U-Pb ages of Vaks et al.,

139   2013 are indicated. In-situ flowstone within Ashalim Cave from which ASH-15 was sampled,

140   showing the large reservoir of this flowstone.

141

3. Sample ASH-15 textural characterization

The ASH-15 thin-section includes section D and E of the ASH-15 sample (see location in Fig.1a). Overall the thin-section examination indicates that the original texture is preserved with consistent growth direction, no observed hiatus, and no indications for dissolution and recrystallization. A spot analysis array, 85 µm in diameter, targeted along growth bands and perpendicular to growth are visible in Fig. 2a-c. The ASH-15 sample shows no luminescence under cathodoluminescence light (Fig. 2c), suggesting formation under oxidising conditions. The slight bright luminescence observed within grain boundaries, discontinuities, and veins (arrows in Fig. 2b-c) may suggest for the presence of fluid inclusions, textural differences, or some local replacement within these areas. These areas should be avoided if possible during spot analysis. The relatively homogenous low luminescence may suggest for a single-phase continuous calcite growth, whereby precipitation occurred relatively rapid from the same fluid source (e.g. with consistent Mn^{2+} Fe^{2+} composition) and/or under similar precipitation redox conditions. This 15 cm thick, ~3 Ma Pliocene layer (section D-K) is essentially of the same age. For this reason, previous dating of this sample also considered a similar initial $^{234}U/^{238}U$ activity ratio for disequilibrium correction (Mason et al., 2013; Vaks et al., 2013). The ASH-15 reference material consists of the whole Pliocene section that terminates with a sharp transition to the darker Pleistocene layers above it (section A-C; see Fig. 1b). About 3 kg of ASH-15 sample are excavated from the Ashalim Cave (Fig. 1a), and potentially much more can be sampled in the future (we estimate more than 10 kg of sample; Fig. 1b). The ASH-15 flowstone is therefore a good candidate for a reference material because of its large volume, high U concentrations, and potentially homogenous age which will be examine next.

164
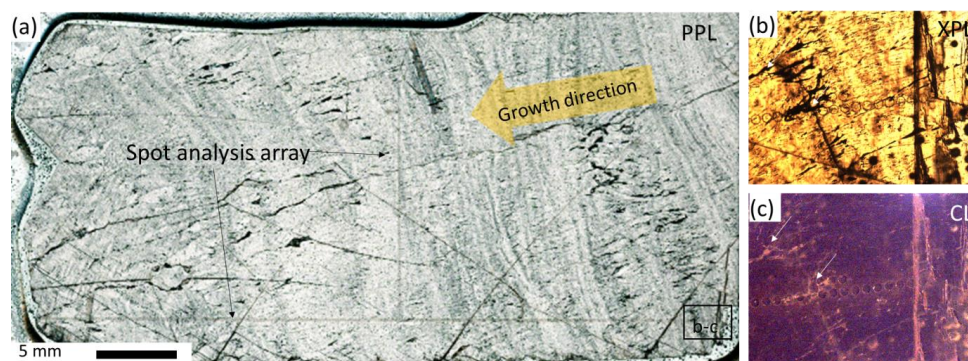
Figure 2. ASH-15D-E thin-section. (a) cross-polarized scan of ASH-15D-E thin-section, 36

mm long, showing continuous growth (no hiatus), and consistent growth direction (indicated

with yellow arrow). Spot analyses are targeted either parallel to growth band or perpendicular

to growth direction,; (b) close-up on spot analyses (location is shown in a) with 85 µm

diameter; (c) CL image of the same area showing no luminescence and some bright

luminescence within grains boundaries and veins (arrows).

4.   Methods

4.1.   Elemental mapping

The sample ASH-15 was cut perpendicular to the growth bands of section D and E (see

Fig.1b) in order to examine heterogeneities across growth bands and within. Thin-sections

were then examined under plane- and cross-polarized light (XPL/PPL), and

cathodoluminescence (CL) microscopy (Fig. 2). The central part of the thin-section was also

analyzed for elemental distribution of selected elements. The elemental maps were measured

via LA-ICPMS, carried out on a 193 nm ArF excimer laser ablation system (Analyte G2

Teledyne Photon Machines Inc., Bozeman MT) coupled to an ICP-QMS (Agilent 7900,

Agilent Technologies, Santa Clara CA). The laser was equipped with a Photon Machines

HelEx II ablation chamber and an Aerosol Rapid Introduction System (ARIS). The

experiments were carried out using acquisition parameters (both on the ICP and on the laser)

183   modelled using the approach of van Elteren et al (2019; 2018) to avoid artefacts (e.g., aliasing,

184   smear, blur). All images (500x500 pixels) were acquired using a 20 µm square beam, fluence

185   of 3.5 Jcm^{-2}, 294 Hz repetition rate and dosage of 10 (amounting to a scanning speed of 588

186   µms^{-1}). The masses monitored were ^{24}Mg, ^{55}Mn, ^{63}Cu, ^{85}Rb ^{88}Sr, ^{137}Ba, ^{206}Pb, ^{208}Pb, ^{232}Th,

187   and ^{238}U and the images were constructed using Photon Machines' HDIP data reduction

188   software (van Malderen, 2017).

4.2.   LA-MC-ICPMS spot analyses

190   A thin section of ASH-15 was dated by U-Pb laser ablation multi-collector inductively

191   coupled plasma mass spectrometry (LA-MC-ICPMS) following the method described in

192   Nuriel et al. (2017). A Nu Plasma 3D was employed in conjunction with a Photon Machines

193   Excite 193nm Excimer laser equipped with a HelEex two volume cell. The laser was fired for

194   15 s during analysis, using a rep rate of 10 Hz, a spot size of 85 µm, and a fluence of approx.

195   1 J/cm^{2}. The Nu Plasma 3D allows for the simultaneous acquisition of ^{238}U, ^{235}U, ^{232}Th, ^{208}Pb,

196   ^{207}Pb, ^{206}Pb, ^{204}Pb(+Hg), and ^{202}Hg, where ^{238}U-^{232}Th are measured on Faraday detectors and

197   the low-side masses are measured on Daly detectors. Instrumental mass-bias was corrected

198   using a two-step approach: both the ^{207}Pb/^{206}Pb and ^{206}Pb/^{238}U ratios were first corrected to

199   NIST-614 glass reference material in *Iolite 3* using the geochronology reduction scheme

200   (Paton et al., 2010) to account for both mass-bias (^{207}Pb/^{206}Pb) and instrumental drift

201   (^{207}Pb/^{206}Pb and ^{206}Pb/^{238}U). The Tera-Wasserburg data, output from *Iolite*, was then plotted

202   and ^{206}Pb/^{238}U ratios of all RMs and unknowns were adjusted such that the primary calcite

203   reference material—WC-1—yielded an age of 254 Ma (Roberts et al., 2017). This resulted in

204   accurate dates for both our secondary calcite RM, Duff Brown Tank (64 Ma; Hill et al., 2016)

205   and a zircon RM (Sri Lanka, 564 Ma; Gehrels et al., 2008), of 66.8 ± 3.4 Ma and a

206   ^{207}Pb/^{206}Pb date of a 566.0 ± 2.8 Ma. Uncertainty propagation of individual ratios was

207   assessed by reproducibility of the NIST614 and SL RMs (n=44 in both cases) and added in

208 quadrature such that the MSWD of each weighted average is ≤1 and that the uncertainty is no

209 better than 2% (long-term reproducibility); this resulted in propagated uncertainties of 2.5%

210 and 2% for the $^{206}Pb/^{238}U$ and $^{207}Pb/^{206}Pb$ ratios, respectively. Given that the typical

211 uncertainties of the $^{206}Pb/^{238}U$ and $^{207}Pb/^{206}Pb$ ratios of the unknowns was >10% and >3%,

212 respectively, the uncertainty propagation on individual ratios had little effect on the

213 calculation of the final date of ASH-15. The thin section of ASH-15 was measured both

214 parallel to the length of section (303 spots, and perpendicular to it (101 spots). Data are

215 plotted using Isoplot (Ludwig, 1998).

216 **4.3.   LA-ICPMS spot analyses**

217 Analyses were conducted at the Geochronology and Tracers Facility, British Geological

218 Survey (Nottingham, UK). The instrumentation comprised a New Wave Research 193UC

219 excimer laser ablation system fitted with a TV2 cell, coupled to a Nu Instruments Attom

220 single collector inductively coupled plasma mass spectrometer (ICP-MS). The method

221 follows the protocols described in Roberts and Walker (2016) and Roberts et al. (2017). Laser

222 parameters varied slightly per session, but typically involve a pre-ablation cleaning spot of

223 150 μm, fired at 10 Hz with a fluence of ~6 J/cm^2 for 2 seconds, and ablation conditions of

224 80-100 μm spots, fired at 10 Hz with a fluence of ~6-8 J/cm^2 for 25-30 seconds. A 60 second

225 background is taken before every set of standard-bracketed analyses, and a 5 second washout

226 is left between each ablation. Normalization of Pb-Pb ratios is achieved using NIST614 glass

227 (values of Woodhead and Hergt, 2001), and WC-1 carbonate for Pb-U ratios (Roberts et al.,

228 2017). Data reduction uses the Time Resolved Analysis function of the Nu Instruments

229 Attolab software, and an excel spreadsheet, with uncertainty propagation following the

230 recommendations of Horstwood et al. (2016).

231

4.4. ID-TIMS U-Pb geochronology

232

233 Isotope dilution thermal ionization mass spectrometry (ID-TIMS) U-Pb geochronology was

234 performed at the Institute of Geochemistry and Petrology of ETH Zurich (ETHZ) and at the

235 Department of Earth Sciences of the University of Geneva (UNIGE). Millimeter-sized chips

236 of the ASH-15-D and ASH-15-K calcite were extracted using stainless steel tools. Larger

237 chips were further sub-divided resulting in ~1-7 mg aliquots. Individual chips were

238 transferred into 3 ml Savillex beakers and repeatedly ultrasonically cleaned in ultrapure

239 acetone and water. Cleaned sampled were transferred into pre-cleaned 3 ml Savillex beakers,

240 spiked with ~5-10 mg EARTHTIME $(^{202}Pb\text{-})^{205}Pb\text{-}^{233}U\text{-}^{235}U$ tracer solution (Condon et al.,

241 2015) and dissolved in 6N HCl at 120°C on a hotplate for ~30 minutes to assure complete

242 dissolution and sample-spike equilibration. Dissolved samples were dried down and

243 redissolved in 1N HBr. Uranium and Pb were separated using a single-column (50 μl, AG1-

244 X8 resin) HBr-HCl anion exchange chemistry. The Pb fraction was dried down with a drop of

245 H_3PO_4 after a single column pass. Uranium was dried down, redissolved in 3N HCl and

246 further purified with a HCl-based second column pass before drying it down with a drop of

247 H_3PO_4. Uranium and Pb were loaded on outgassed single Re filaments with ~1 μl of Si-gel

248 emitter for thermal ionization mass spectrometry. Uranium and Pb isotope ratios were

249 measured on a Thermo TRITON Plus at ETHZ and a Thermo TRITON at UNIGE. Lead

250 isotopes were measured on the axial secondary electron multiplier employing dynamic peak-

251 hopping routine collecting masses (202), 204, 205, 206, 207 and 208. Measured Pb isotope

252 ratios were corrected for mass fractionation either using the double spike (ETHZ) or using a

253 mass fractionation factor of 0.15 ± 0.03 %/amu for single Pb spiked samples (UNIGE).

254 Uranium isotope ratios were measured as uranium-oxide (UO_2) employing a static

255 measurement routine with Faraday cups connected to amplifiers with 10^{13} ohm feedback

256 resistors (von Quadt et al., 2016; Wotzlaw et al., 2017). Isotope ratios were corrected for

257 isobaric interferences from minor UO$_2$ isotopologues (Wotzlaw et al., 2017) and for mass

258 fractionation using the double spike assuming a ^{238}U/^{235}U ratio of 137.818 ± 0.045 (Hiess et

259 al., 2012) for sample and blank. Total procedural Pb blanks for the HBr-based chemistry at

260 ETHZ are consistently between 0.2 and 0.4 pg. We therefore attribute up to 0.4 pg to

261 laboratory blank with the remaining common Pb being attributed to initial common Pb. Total

262 procedural blanks measured at UNIGE yielded an average of 1.15 pg that was taken as the

263 laboratory blank contribution. Data reduction and uncertainty propagation was performed

264 using Tripoli and an Microsoft Excel-based spreadsheet that uses the algorithms of Schmitz

265 and Schoene (2007). Isochron calculations were performed using IsoplotR (Vermeesch,

266 2018). All uncertainties are reported at 95% confidence ignoring systematic uncertainties

267 associated with the tracer calibration and decay constants unless otherwise stated.

268 **5. Results**

269 All analyses were performed on ASH-15-D-K yellow Pliocene layer, abbreviated here as

270 "ASH-15" unless specification of ASH-15-D, E etc. is indicated. The ASH-15-A-C brown

271 Pleistocene layer is not part of the ASH-15 suggested reference material.

272 **5.1. LA elemental mapping**

273 Elemental mapping for ^{88}Sr, ^{137}Ba, ^{206}Pb, ^{208}Pb, ^{238}U and ^{238}U/^{206}Pb ratio shows that the

274 distribution of most elements is relatively homogeneous (Fig.3), and in good accordance with

275 the luminescence data. Higher intensities for ^{238}U and ^{88}Sr were observed along grain

276 boundaries and discontinuities, whereas Pb and the rest of the trace elements are more

277 homogeneously distributed arguing for environmental conditions that have kept steady during

278 the deposition. Ten random regions of interest (ROI) were selected throughout the sample to

279 mimic 10 spot analysis carried out at 85-90 microns spot size – just like one would do for U-

280 Pb geochronology, for example. These ROIs were generated by drawing on the map circular

281 regions with the radius of 85 or 90 microns in diameter. The pixels comprising each ROI

282 were pooled together as representing the equivalent of a single spot analysis. The statistical

283 data for each cluster (data are given in supplementary file) was compared. The average values

284 for all pixel data is within 2 standard errors and in good agreement, indicating that at least

285 based on the elemental distribution we measured, the sample is relatively homogeneous for a

286 natural sample. To further investigate the chemical homogeneity of the sample, a random

287 transect through one of the growth zones was drawn and the signal intensities for ^{238}U were

288 extracted. The transect data also indicate that ^{238}U variations are within 2 standard errors of

289 the average value.
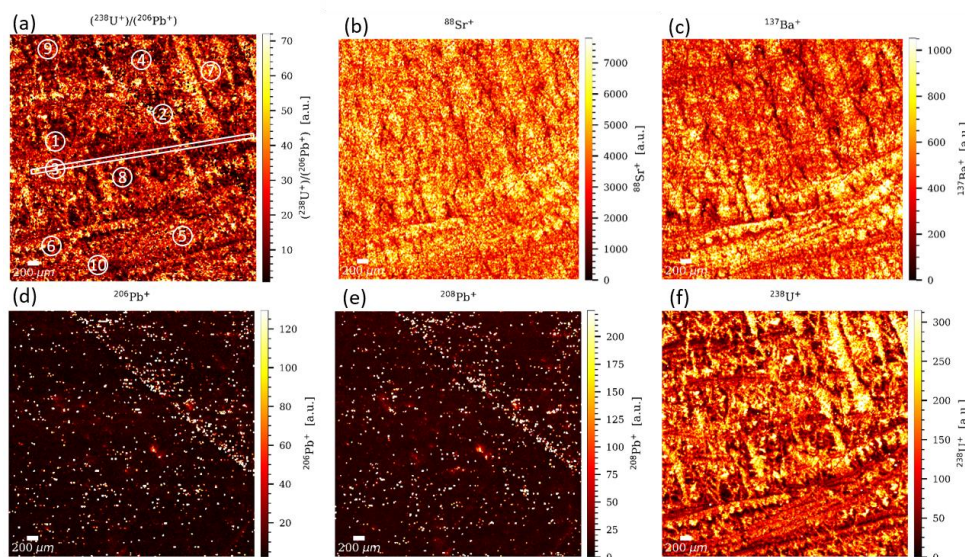
290

291 **Figure 3.** Signal intensity maps of ASH-15. for ^{238}U/^{206}Pb, ^{88}Sr, ^{137}Ba, ^{206}Pb, ^{208}Pb, and ^{238}U

292 (a-d). The plotted signal was corrected for blank and analytical drift of the instrumentation.

293 Note that each distribution map has its own signal intensity scale. The position of the regions

294 of interest and transect is shown in (a). The circles designating the location of the regions of

295 interest are not at scale.

5.2. LA-MC-ICPMS spot analyses

296

297 Data and calculated ages for the LA-ICPMS transects are shown in Tera-Wasserburg space in

298 Fig. 4 (n = 379 of 412 total spots). Analyses rejected from the age calculation include those

299 with $^{207}Pb/^{206}Pb$ uncertainties larger than 0.1 (n = 2) and those with high common-Pb

300 contents (^{208}Pb cps >5000; n = 17). A further 14 spots plotted below the array; these data

301 were the first 1–2 mm of spots of the lengthwise transect (lower right in Fig. 2a), and suggest

302 that a small percent of ASH-15 may behave differently during ablation and/or may have been

303 subsequently modified after crystallization; upon inspection, this portion of the section

304 contains more pore space and impurities than the majority of the section. The remaining 379

305 define a normally distributed array with a lower intercept age of 2.952 ± 0.043 Ma (MSWD =

306 2.5), which is well within uncertainty of the new ID-TIMS data presented herein and the

307 scatter observed in the LA data (i.e., MSWD > 1) is lower compared with scatter observed in

308 the ID-TIMS data. The calculated upper intercept of each transect is equivalent and within

309 1% of the common Pb composition calculated from the ID-TIMS data. Not surprisingly, the

310 lengthwise transect reveals a larger spread in common/radiogenic Pb ratios; this transect

311 crosses more growth zones and has a higher probability of sampling a variety of

312 concentrations of both Pb and U. Conversely, the more limited spread in common/radiogenic

313 Pb ratios appears to reflect the limited sampling of growth zones, and would suggest that

314 individual growth zones contain a relatively limited range of concentrations in U and Pb. The

315 slightly higher MSWD for the lengthwise transect (2.7) relative to the growth zone transect

316 (2.5) could also reflect these inherited compositional differences during growth history, and a

317 resulted "mixing" or "averaging" of different growth phase along calcite continuous growth.

318 Variations of ASH-15 ages during 20 different runs using both single (ICPMS) and multi-

319 collector (MC-ICPM) are shown in Fig. 4b. The ages are calculated using IsoplotR, anchored

320 to 0.8315 common-lead, and are not corrected for disequilibrium. Although there is a large

321 scatter in the ages of the different runs the average ages (marked in thick lines) are plotted

322 close to the new ID-TIMS ages, or slightly younger in age.

323
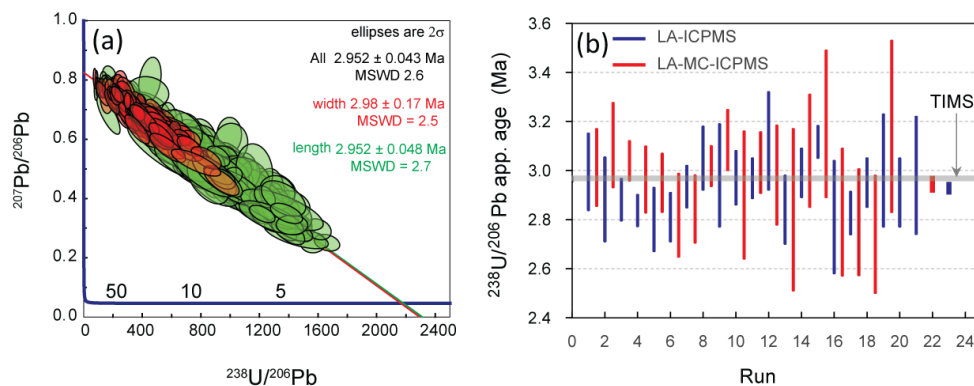
Figure 4. LA-MC-ICPMS analyses of calcite ASH-15 (n=385). Spots within lengthwise

325 transect (green) and along growth zone transect (red). Calculated age, 2σ error and MSWD

326 are given for both and for all spots together; (b) Variations of ASH-15 ages during different

327 runs using both single and multi-collector ICPMS. Ages are calculated using WC1 as primary

328 MS; the new ID-TIMS age is indicated with a grey line; Ages are calculated using IsoplotR,

329 anchored to 0.8315 common-lead, and are not corrected for disequilibrium.

5.3. Down-hole fractionation

331 Reference material is important for correction of both laser-induced elemental fractionation

332 (LIEF) and in plasma-related ionization efficiency. Ideally, the reference material should

333 resemble the unknown samples as much as possible in terms of its chemistry (e.g. Mg and Fe

334 content), texture (i.e. micritic, crystalline), and age. The WC1 and ASH15 are both low-Mg

335 calcite but they are very different in their textures and age. The ASH15 is a ~3 Ma, well-

336 crystallized elongated calcite (up to 1 cm) and WC1 is a 254 Ma recrystallized botryoidal

337 calcite, formed after aragonite. Despite these differences, both WC1 and ASH15 display a

338 very similar down-hole fractionation pattern (Fig. 5d). Fig. 5 shows stacked integration plots

339 of the down-hole raw ^{206}Pb/ ^{238}U ratio of different RMs including, the ASH15, WC-1, and

340 Duff Brown Tank (Black and Gulson, 1978). The ASH15 display much larger scatter in the

341 raw data (Fig. 5a) in comparison to both WC1 and Duff Brown Tank (Fig. 5b-c), however,

342 the average value yielded identical down-hole patterns to that of WC-1 (Fig. 5d). Duff Brown

343 Tank is also consistent with the down-hole patterns bet less steep in comparison to WC1 and

344 ASH15 (Fig. 5d). This comparison suggest that down-hole fractionation and laser-induced

345 elemental fractionation (LIEF) is similar among the different RMs. It is thus suggested that

346 differences in ^{206}Pb/^{238}U ratios between measured and expected in calcite material are likely

347 to be caused mostly by plasma-ionization differences between unknown samples and RMs.
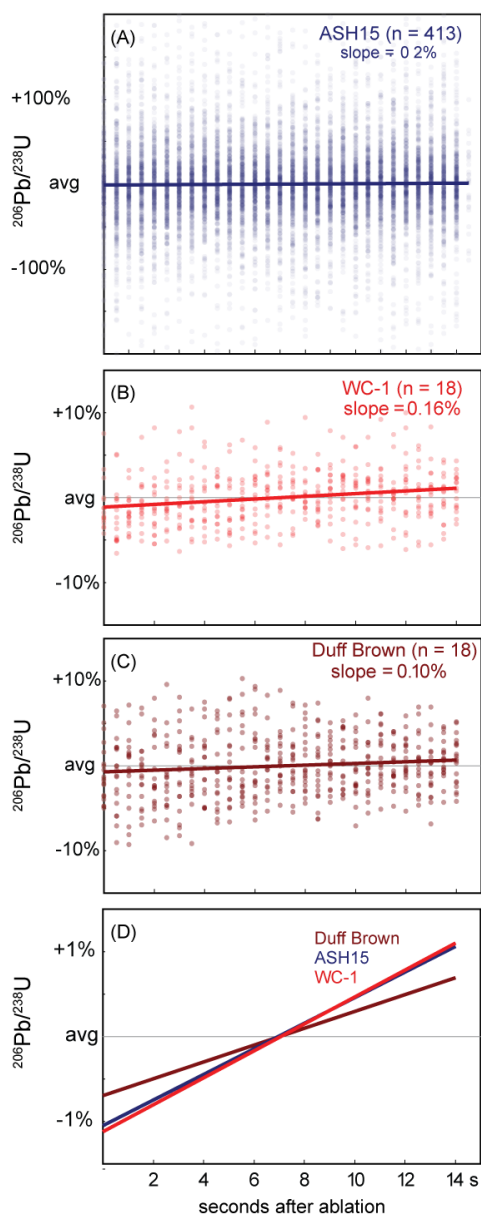
Figure 5. Stacked integration plots of raw [207]Pb-corrected [206]Pb/[238]U ratios for calcite reference materials ASH-15, WC-1, and Duff Brown Tank. The low Pb concentration in ASH-15 yields more scatter, but average slopes of all RMs are similar, with 1-2% change in age over 10 seconds (100 pulses) of ablation. The results suggest for minimal differences in down-hole fractionation of the different RMs.

5.4. High-precision ID-TIMS results

354

355 Twelve aliquots of ASH-15D analyzed at ETHZ yielded $^{238}U/^{206}Pb$ ratios between 1096 and

356 2084 and $^{207}Pb/^{206}Pb$ ratios between 0.0825 and 0.4403. Plotted in Tera-Wasserburg space,

357 this data yields a single isochron with an initial $^{207}Pb/^{206}Pb$ of 0.832 ± 0.015 (uncertainties are

358 95% confidence intervals) and a concordia intercept age of 2.967 ± 0.022 Ma (Fig. 6a). The

359 elevated mean square weighted deviation (MSWD) of 12 is attributed to minor

360 heterogeneities, most likely in the initial $^{207}Pb/^{206}Pb$ ratio of the speleothem calcite. Twelve

361 aliquots of ASH-15K analysed at ETHZ returned $^{238}U/^{206}Pb$ ratios between 723 and 2094 and

362 $^{207}Pb/^{206}Pb$ ratios between 0.0720 and 0.5677. In Tera-Wasserburg space, eleven out of

363 twelve aliquots define a isochon with an initial $^{207}Pb/^{206}Pb$ of 0.8314 ± 0.0040 and a

364 concordia intercept age of 2.964 ± 0.016 Ma (Fig. 6b). A single aliquot (#5.4) plots

365 significantly below the isochron defined by the other aliquots. The elevated MSWD of 34

366 together with the single outlier suggest some heterogeneities in the initial $^{207}Pb/^{206}Pb$ of the

367 ASH-15K calcite. Thirteen aliquots of ASH-15K analysed at UNIGE (pink color, Fig. 6b)

368 yielded $^{238}U/^{206}Pb$ ratios between 433 and 1853 and and $^{207}Pb/^{206}Pb$ ratios ranging from

369 0.1856 to 0.6660. Twelve of the thirteen analyses yield define an isochron with an initial

370 $^{207}Pb/^{206}Pb$ of 0.814 ± 0.019 and a Concordia intercept age of 2.947 ± 0.065 Ma. The elevated

371 MSWD of 36 confirms the minor heterogeneity of the initial $^{207}Pb/^{206}Pb$.

372 The excellent agreement between the ASH-15D and ASH-15K datasets suggest that the entire

373 speleothem growth layer between these two growth zones is of equivalent age with minor

374 heterogeneities in the initial $^{207}Pb/^{206}Pb$ ratio and justifies combining the data into a single

375 isochron regression. The combined isochron, using 35 of 37 analysed aliquots, yields an

376 initial $^{207}Pb/^{206}Pb$ of 0.8306 ± 0.0033 and a concordia intercept age of 2.965 ± 0.011 Ma with

377 a MSWD of 35 (Fig. 6c). We consider the results of the combined isochron regression as the

378 best reference value for using ASH-15 as a primary reference material.

379   The new TIMS data provide the most extended bulk-analyses work of the ASH-15 sample,

380   with a total of 37 sub-samples that are separated from bottom (K, n=25) to top (D, n=12)

381   sections of the sample. The relatively high MSWD of 35 is suggested to reflect true

382   heterogeneities of the dated material, possibly related to impurities that are concentrated

383   within grain boundaries (as suggested by CL and elemental mapping). We re-calculated

384   previously determined isochron ages of Vaks et al. (2013) and Mason et al. (2013; Fig. 7).

385   We obtained concordia intercept ages of 3.0088 ± 0.053 Ma for ASH-15-D (MSWD=11;

386   n=5) and 3.0153 ± 0.042 Ma for ASH-15-K (MSWD=14; n=5) of Vaks et al. (2013) and

387   3.0015 ± 0.029 for ASH-15-D (MSWD=2; n=5) of Mason et al. (2013). These ages are

388   systematically older but still overlap within uncertainty with our new age of 2.965 ± 0.011

389   Ma (Fig. 7). We speculate that the small but systematic offset between previous results and

390   our new data may be related to natural heterogeneities that are sampled differently depending

391   on sample size but we cannot exclude analytical differences as an additional source of bias.

392   The origin of this bias between the two techniques should be investigated more

393   systematically in future. For laser ablation U-Pb work, we recommend the use of the new ID-

394   TIMS age because of the large number of sub-samples (n=37), and the small aliquots (1-7

395   mg) that are more representative of laser-ablation spot analysis. In addition, the use of the

396   precisely and accurately calibrated EARTHTIME tracer solutions (Condon et al., 2015) and

397   the online mass fractionation correction provided by the double Pb and double U tracer are an

398   important advantage of this method compared to previous bulk analyses. The excellent

399   interlaboratory reproducibility gives us additional confidences that our ID-TIMS data provide

400   the most accurate characterization of the U-Pb systematics of the ASH-15 calcite for use as a

401   primary reference material.
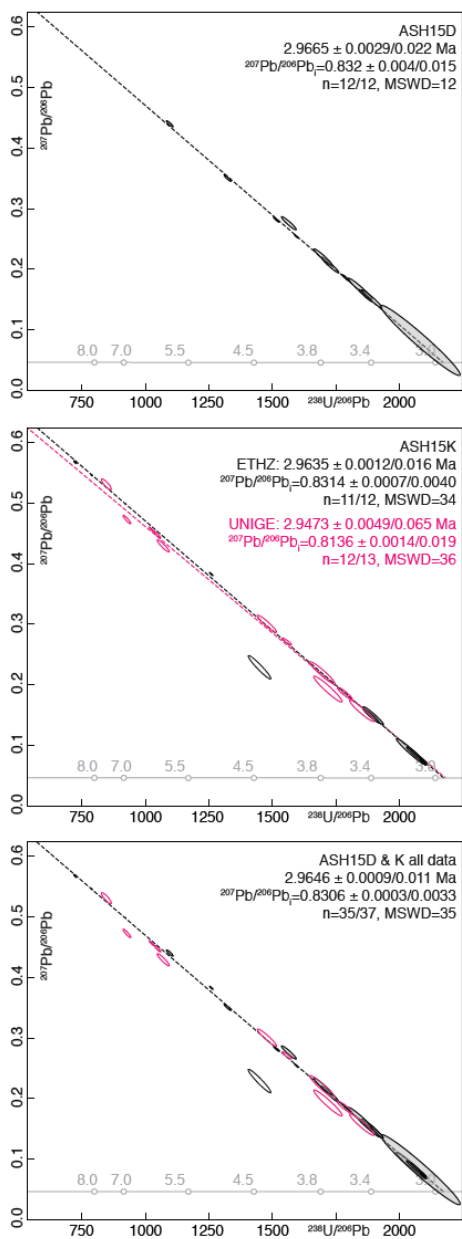
Figure 6. ID-TIMS U-Pb results for ASH-15D, ASH-15K, and for both ASH-15D +K.
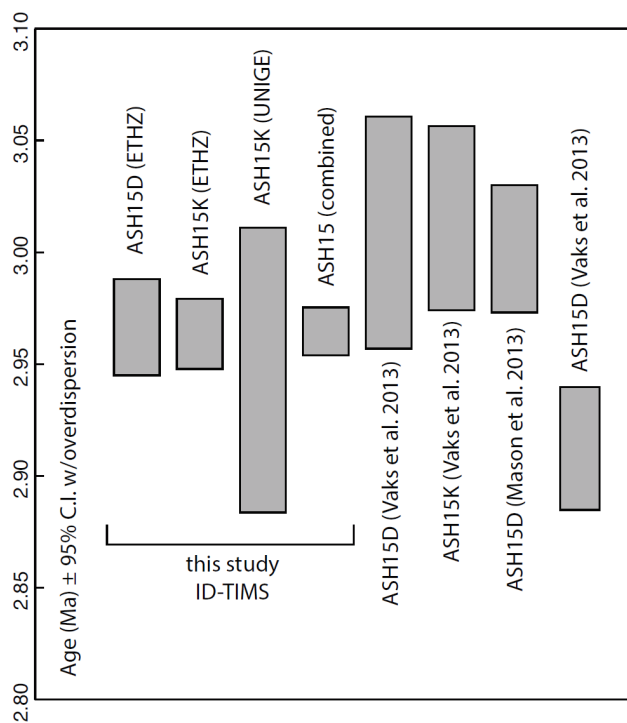
Figure 7. Previous (re-calculated) and new ages of ASH-15 from isotope-dilution U-Pb analysis. All ages are calculated using IsoplotR and are not corrected for disequilibrium and are not anchored to common-lead specific value.

6. Conclusions

The ASH-15 speleothem calcite is characterized as a matrix matched reference material for LA-ICPMS U-Pb geochronology of calcite. ID-TIMS analyses of small 1-7 mg aliquots of two growth zones suggest sufficient homogeneity with a combined intercept age of 2.965 ± 0.011 Ma and an initial $^{207}Pb/^{206}Pb$ of 0.8315 ± 0.0026. These data are recommended as the reference values for the ASH-15 calcite reference material. The excellent agreement between the two growth zones suggest that the entire interval between the two dated layers can be used with the same reference age. Compared to other calcite reference material (e.g. WC1),

416   ASH-15 is more homogeneous but has lower radiogenic Pb content and therefore requires

417   more sensitive instruments (i.e. sector field rather than quadrupole mass spectrometers) to be

418   used as a reference material.

Table 1. U-Th-Pb isotopic data

Sample	Wt. mg	U ppm	Pb ppm	Th/U	^{206}Pb* x10^{-13} mol	mol % ^{206}Pb*	Pb*/Pbc	Pbc (pg)	$\frac{^{206}Pb}{^{204}Pb}$
(a)	(b)	(c)	(c)	(d)	(e)	(e)	(e)	(e)	(f)
ASH-15D (ETHZ)									
2	2.165	2.24	0.002	0.009	0.0931	82.28%	1.23	1.63	105
3	2.392	1.26	0.001	-	0.0569	66.53%	0.52	2.34	56
5	4.085	1.80	0.001	0.010	0.1409	80.14%	1.07	2.85	94
6	5.446	1.99	0.002	0.020	0.2110	73.23%	0.73	6.31	70
8	3.994	1.90	0.002	0.018	0.1466	68.61%	0.58	5.49	60
10	1.523	2.15	0.002	-	0.0625	80.81%	1.10	1.21	97
11	1.600	1.70	0.001	0.015	0.0519	78.34%	0.96	1.17	86
12	0.965	1.18	0.001	0.039	0.0218	78.32%	0.98	0.48	85
13	1.776	1.95	0.002	0.022	0.0666	75.21%	0.81	1.79	75
14	2.470	1.90	0.003	0.022	0.0908	59.47%	0.39	5.06	46
16	1.827	1.65	0.003	0.014	0.0577	48.13%	0.25	5.09	36
17	1.680	1.96	0.002	0.011	0.0632	73.55%	0.74	1.85	71
ASH-15K (ETHZ)									
3.1	3.025	9.94	0.025	0.033	0.5834	42.70%	0.20	64.16	33
3.2	1.313	2.56	0.009	0.025	0.0662	33.30%	0.13	10.86	28
4.1	3.200	2.62	0.008	-	0.1632	36.38%	0.15	23.39	29
5.1	3.662	2.28	0.004	0.036	0.1593	56.52%	0.35	10.04	43
5.2	2.229	1.17	0.001	0.019	0.0504	86.50%	1.72	0.63	138
5.3	1.548	2.13	0.002	0.030	0.0631	81.40%	1.17	1.17	100
5.4 (j)	*1.221*	*1.42*	*0.002*	*0.021*	*0.0383*	*69.98%*	*0.62*	*1.34*	*62*
7.1	2.108	2.47	0.001	-	0.1003	90.66%	2.58	0.84	199
7.2	2.595	2.94	0.002	0.010	0.1467	92.03%	3.08	1.03	234
9.1	3.125	1.30	0.001	0.000	0.0778	82.46%	1.25	1.35	106
10.1	2.525	4.77	0.002	0.008	0.2327	94.93%	4.99	1.01	367
10.2	3.269	3.25	0.002	0.003	0.2039	94.08%	4.23	1.04	314
ASH15K (UNIGE)									
2.1	3.3	0.43	0.003	-	0.0293	19.59%	0.06	9.86	23
2.2	2.0	3.83	0.003	-	0.1483	79.60%	1.02	3.11	91
2.4 (j)	*4.5*	*3.12*	*0.016*	*-*	*0.2031*	*18.93%*	*0.03*	*71.29*	*23*
2.5	2.1	2.67	0.003	-	0.1108	73.96%	0.74	3.20	72
6.1	2.5	2.47	0.003	-	0.1184	71.35%	0.64	3.90	65
6.2	7.3	2.38	0.003	-	0.3346	69.67%	0.60	11.94	62
6.3	2.8	2.25	0.003	-	0.1207	62.96%	0.44	5.82	50
6.4	5.0	2.53	0.002	-	0.2440	78.69%	0.97	5.42	88
6.5	1.9	2.10	0.007	-	0.0761	36.09%	0.14	11.05	29
9.2	2.7	7.08	0.016	-	0.3746	47.26%	0.23	34.27	35
9.3	2.6	2.04	0.004	-	0.1063	48.13%	0.24	9.39	36
9.4	2.5	2.59	0.007	-	0.1347	44.10%	0.20	13.99	33
9.5	2.1	4.90	0.011	-	0.2012	47.43%	0.23	18.28	36

(a) Fractions are single chips of calcite
(b) mass of fraction in mg
(c) U and total Pb concentrations.
(d) Model Th/U ratio iteratively calculated from the radiogenic ^{208}Pb/^{206}Pb ratio and ^{206}Pb/^{238}U age.
    Fractions without value (-) have ^{208}Pb/^{204}Pb indistinguishable from common Pb therefore no Th content was calculated.
(e) Pb* and Pbc represent radiogenic and common Pb, respectively; mol % ^{206}Pb* with respect to radiogenic, blank and initial common Pb.
(f) Measured ratio corrected for spike and fractionation only.
(g) Corrected for fractionation, spike, and blank Pb only.
(h) Errors are 2-sigma, propagated using the algorithms of Schmitz and Schoene (2007).
(g) Isochron age calculations are based on the decay constants of Jaffey et al. (1971).
(j) Fraction excluded from isochron regressions

419

420 **Appendices**
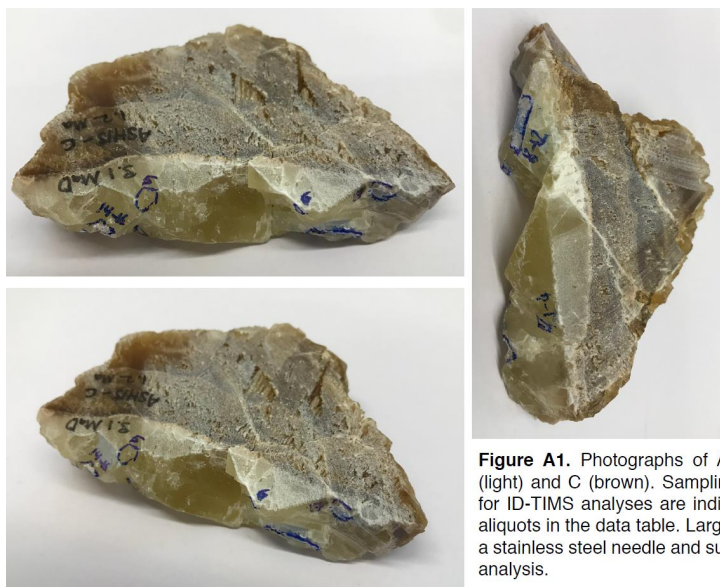
Figure A1. Photographs of ASH15 flowstone with layers D (light) and C (brown). Sampling localities of aliquots sampled for ID-TIMS analyses are indicated by numbers matching the aliquots in the data table. Larger pieces were chipped off using a stainless steel needle and subdivided into smaller aliquots for analysis.

421

Figure A2. Photographs of ASH15 flowstone with layers K (bottom) to D (top). Sampling localities of aliquots samples for ID-TIMS analyses within layer K are indicated with numbers (n=12) and are matching the aliquots in the data table.

422

References:

Anjiang, S., Anping, H., Cheng, T., Liang, F., Wenqing, P., Yuexing, F., and Zhao, J.: Laser ablation in situ U-Pb dating and its application to diagenesis-porosity evolution of carbonate reservoirs, 46, 1127-1140, 2019.

Condon, D., Schoene, B., McLean, N., Bowring, S., and Parrish, R.: Metrology and traceability of U– Pb isotope dilution geochronology (EARTHTIME Tracer Calibration Part I), Geochimica et Cosmochimica Acta, 164, 464-480, 2015.

Coogan, L. A., Parrish, R. R., and Roberts, N. M.: Early hydrothermal carbon uptake by the upper oceanic crust: Insight from in situ U-Pb dating, Geology, 44, 147-150, 2016.

Crouvi, O., Amit, R., Enzel, Y., and Gillespie, A. R.: Active sand seas and the formation of desert loess, Quaternary Science Reviews, 29, 2087-2098, 2010.

Godeau, N., Deschamps, P., Guihou, A., Leonide, P., Tendil, A., Gerdes, A., Hamelin, B., and Girard, J.-P. J. G.: U-Pb dating of calcite cement and diagenetic history in microporous carbonate reservoirs: Case of the Urgonian Limestone, France, 46, 247-250, 2018.

Guillong, M., Wotzlaw, J. F., Looser, N., and Laurent, O.: New analytical and data evaluation protocols to improve the reliability of U-Pb LA-ICP-MS carbonate dating, Geochronology Discuss., 2020, 1-17, 10.5194/gchron-2019-20, 2020.

Hansman, R. J., Albert, R., Gerdes, A., and Ring, U.: Absolute ages of multiple generations of brittle structures by U-Pb dating of calcite, Geology, 46, 207-210, 2018.

Hiess, J., Condon, D. J., McLean, N., and Noble, S. R.: 238U/235U systematics in terrestrial uranium-bearing minerals, Science, 335, 1610-1614, 2012.

Holdsworth, R., McCaffrey, K., Dempsey, E., Roberts, N., Hardman, K., Morton, A., Feely, M., Hunt, J., Conway, A., and Robertson, A.: Natural fracture propping and earthquake-induced oil migration in fractured basement reservoirs, Geology, 47, 700-704, 2019.

Horstwood, M. S., Košler, J., Gehrels, G., Jackson, S. E., McLean, N. M., Paton, C., Pearson, N. J., Sircombe, K., Sylvester, P., and Vermeesch, P.: Community- derived standards for LA-ICP-MS U-(Th-) Pb geochronology–Uncertainty propagation, age interpretation and data reporting, Geostandards and Geoanalytical Research, 40, 311-332, 2016.

Li, Q., Parrish, R., Horstwood, M., and McArthur, J.: U–Pb dating of cements in Mesozoic ammonites, Chemical Geology, 376, 76-83, 2014.

Lisiecki, L. E., and Raymo, M. E.: A Pliocene-Pleistocene stack of 57 globally distributed benthic $\delta^{18}O$ records, Paleoceanography, 20, 2005.

MacDonald, J., Faithfull, J., Roberts, N., Davies, A., Holdsworth, C., Newton, M., Williamson, S., Boyce, A., John, C. J. C. t. M., and Petrology: Clumped-isotope palaeothermometry and LA-ICP-MS U–Pb dating of lava-pile hydrothermal calcite veins, 174, 63, 2019.

Mason, A. J., Henderson, G. M., and Vaks, A.: An Acetic Acid-Based Extraction Protocol for the Recovery of U, Th and Pb from Calcium Carbonates for U-(Th)-Pb Geochronology, Geostandards and Geoanalytical Research, 37, 261-275, 10.1111/j.1751-908X.2013.00219.x, 2013.

461   Nuriel, P., Weinberger, R., Kylander-Clark, A. R. C., Hacker, B. R., and Craddock, J. P.: The onset of
462   the Dead Sea transform based on calcite age-strain analyses, Geology, *45*, 587-590, 10.1130/g38903.1,
463   2017.

464   Nuriel, P., Craddock, J., Kylander-Clark, A. R., Uysal, I. T., Karabacak, V., Dirik, R. K., Hacker, B.
465   R., and Weinberger, R. J. G.: Reactivation history of the North Anatolian fault zone based on calcite
466   age-strain analyses, 47, 465-469, 2019.

467   Parrish, R. R., Parrish, C. M., and Lasalle, S.: Vein calcite dating reveals Pyrenean orogen as cause of
468   Paleogene deformation in southern England, Journal of the Geological Society, 10.1144/jgs2017-107,
469   2018.

470   Piccione, G., Rasbury, E. T., Elliott, B. A., Kyle, J. R., Jaret, S. J., Acerbo, A. S., Lanzirotti, A.,
471   Northrup, P., Wooton, K., and Parrish, R. R.: Vein fluorite U-Pb dating demonstrates post–6.2 Ma
472   rare-earth element mobilization associated with Rio Grande rifting, Geosphere, 15, 1958-1972, 2019.

473   Ring, U., and Gerdes, A.: Kinematics of the Alpenrhein-Bodensee graben system in the Central Alps:
474   Oligocene/Miocene transtension due to formation of the Western Alps arc, Tectonics, 35, 1367-1391,
475   10.1002/2015TC004085/abstract, 2016.

476   Roberts, N. M., and Walker, R. J.: U-Pb geochronology of calcite-mineralized faults: Absolute timing
477   of rift-related fault events on the northeast Atlantic margin, Geology, 44, 531-534, 2016.

478   Roberts, N. M., Rasbury, E. T., Parrish, R. R., Smith, C. J., Horstwood, M. S., and Condon, D. J.: A
479   calcite reference material for LA-ICP-MS U-Pb geochronology, Geochemistry, Geophysics,
480   Geosystems, 2017.

481   Schmitz, M. D., and Schoene, B.: Derivation of isotope ratios, errors, and error correlations for U-Pb
482   geochronology using ^{205}Pb-^{235}U-(^{233}U)-spiked isotope dilution thermal ionization mass spectrometric
483   data, Geochemistry, Geophysics, Geosystems, 8, 2007.

484   Vaks, A., Bar-Matthews, M., Matthews, A., Ayalon, A., and Frumkin, A.: Middle-Late Quaternary
485   paleoclimate of northern margins of the Saharan-Arabian Desert: reconstruction from speleothems of
486   Negev Desert, Israel, Quaternary Science Reviews, 29, 2647-2662, 2010.

487   Vaks, A., Woodhead, J., Bar-Matthews, M., Ayalon, A., Cliff, R. A., Zilberman, T., Matthews, A.,
488   and Frumkin, A.: Pliocene–Pleistocene climate of the northern margin of Saharan–Arabian Desert
489   recorded in speleothems from the Negev Desert, Israel, Earth and Planetary Science Letters, 368, 88-
490   100, http://dx.doi.org/10.1016/j.epsl.2013.02.027, 2013.

491   Vaks, A., Bar-Matthews, M., Ayalon, A., Matthews., A., Frumkin, A. Pliocene − Pleistocene
492   paleoclimate reconstruction from Ashalim Cave speleothems, Negev Desert, Israel., In: Parise, M.,
493   Gabrovsek, F., Kaufmann, G. & Ravbar, N. (eds) Advances in Karst Research: Theory, Fieldwork and
494   Applications. Geological Society, London, Special Publications, 466 (1), pp. 201-206, 2018.

495   van Elteren, J. T., Šelih, V. S., Šala, M., Van Malderen, S. J., and Vanhaecke, F.: Imaging artifacts in
496   continuous scanning 2D LA-ICPMS imaging due to nonsynchronization issues, Analytical chemistry,
497   90, 2896-2901, 2018.

498   van Elteren, J. T., Šelih, V. S., and Šala, M.: Insights into the selection of 2D LA-ICP-MS (multi)
499   elemental mapping conditions, Journal of Analytical Atomic Spectrometry, 34, 1919-1931, 2019.

500   van Malderen, S.: Optimization of methods based on laser ablation-ICP-mass spectrometry (LA-ICP-
501   MS) for 2-D and 3-D elemental mapping, Ghent University, 2017.

502 Vermeesch, P.: IsoplotR: A free and open toolbox for geochronology, Geoscience Frontiers, 2018.

503 von Quadt, A., Wotzlaw, J.-F., Buret, Y., Large, S. J., Peytcheva, I., and Trinquier, A.: High-precision
504 zircon U/Pb geochronology by ID-TIMS using new 10 13 ohm resistors, Journal of Analytical Atomic
505 Spectrometry, 31, 658-665, 2016.

506 Woodhead, J., and Petrus, J. J. G.: Exploring the advantages and limitations of in situ U–Pb carbonate
507 geochronology using speleothems, 1, 69-84, 2019.

508 Woodhead, J. D., and Hergt, J. M.: Strontium, neodymium and lead isotope analyses of NIST glass
509 certified reference materials: SRM 610, 612, 614, Geostandards Newsletter, 25, 261-266, 2001.

510 Wotzlaw, J.-F., Buret, Y., Large, S. J., Szymanowski, D., and von Quadt, A.: ID-TIMS U–Pb
511 geochronology at the 0.1‰ level using 10 13 Ω resistors and simultaneous U and $^{18}O/^{16}O$ isotope
512 ratio determination for accurate UO_2 interference correction, Journal of Analytical Atomic
513 Spectrometry, 32, 579-586, 2017.